Microstructure Refinement of Nd-Fe-B Permanent Magnets Prepared via Spark-Plasma Sintering

T. Tomše

Department for Nanostructured Materials, Jožef Stefan Institute, 1000 Ljubljana, Slovenia

Sintered Nd-Fe-B-type permanent magnets are normally manufactured using a conventional powder-metallurgy approach. The limitations of such high-temperature, pressureless sintering methods include restricted control over the microstructure due to grain growth and constraints on the magnet's geometry. The modern spark-plasma sintering (SPS) technique employs Joule heating and external pressure to offer lower consolidation temperatures and faster heating cycles compared to conventional approaches. As a result, the SPS has the potential for the rapid, low-temperature, net-shape manufacture of magnets. However, the nonequilibrium conditions associated with the SPS can lead to poor grain-boundary wetting and the formation of the soft-magnetic α-iron phase in samples prepared from anisotropic, microcrystalline Nd-Fe-B powders produced by standard procedures, i.e., strip casting, hydrogen decrepitation, and jet-milling. This study revealed that the absence of the Nd-rich grain-boundary film is related to the presence of hydrogen. Degassing the Nd-Fe-B powder before applying the SPS improved the distribution of the grain-boundary phase. Moreover, reducing the electrical currents in the sample during the SPS prevented the decomposition of the $RE_2Fe_{14}B$ matrix, ensuring a favorable phase composition. Compared to magnets conventionally sintered at 1070 °C, the mean grain diameter of the SPS samples prepared at ≈880 °C was reduced by ≈33%. This reduction decreased the temperature coefficient of coercivity from −0.65 to −0.58%/°C. The coercivity increase measured for the SPS samples amounted to more than 15%, which was attributed to the combined effect of smaller grain size and reduced texture.

***Index Terms*— Microstructure refinement, Nd-Fe-B magnets, rapid sintering, spark-plasma sintering (SPS)/field-assisted sintering technique (FAST).**

I. Introduction

SINTERED Nd-Fe-B permanent magnets, with their maximum energy products $(BH)_{max}$ reaching 450 kJ/m^3, are the material of choice for energy-conversion devices [1], [2]. However, their large grain size limits the magnets' high-temperature performance due to their deteriorating effect on the intrinsic coercivity, H_{ci} [3]. Microstructure refinement is crucial to enhancing H_{ci} by minimizing the dipolar interactions [4] and can be partially achieved by introducing advanced milling strategies to obtain finer powders [5]. However, conventional high-temperature sintering is typically in the range of 1000 °C–1100 °C, which results in grain growth. The spark-plasma sintering (SPS), also known as field-assisted sintering technique (FAST), is an electrical-current-activated, pressure-assisted technique that allows for rapid heating rates (several hundred Kelvin per minute) and lower sintering temperatures than conventional, pressureless sintering [6]. SPS utilizes the Joule heating effect, dissipating the heating power directly into the electrically conductive sample, which can promote uniform densification and minimize grain growth. The concept of utilizing the SPS to prepare anisotropic Nd-Fe-B magnets from milled microcrystalline powders was introduced two decades ago [7]. Compared to conventionally sintered magnets, SPS samples have improved corrosion resistance and better mechanical strength, notably a 31% higher impact toughness and a 44% higher bending strength, which the authors attributed to the finer microstructure [7], [8]. It was shown that the mean grain size and the as-sintered density increased with an increasing SPS temperature, with ≈15% smaller grains reported for dense SPS samples, compared to conventionally sintered magnets [9]. However, the final H_{ci} values of the post-sinter annealed SPS samples did not exceed those of conventionally sintered magnets [7], [8], [9]. More recently, it was revealed that the unique nonequilibrium conditions inherent to the SPS, particularly the micro-nonuniform temperature distribution within the sample resulting from localized Joule heating at particle-particle interfaces, can trigger the decomposition of the $RE_2Fe_{14}B$ (RE = rare-earth) phase and the formation of soft-magnetic α-Fe [10]. In addition, the absence of grain-boundary wetting led to exchange coupling among the matrix grains. As a result, the as-sintered H_{ci} values of the samples prepared by the SPS were limited to ≈30 kA/m, necessitating extensive post-SPS tempering, including heating at 1100 °C for 120 min, to achieve the hard-magnetic properties in the final magnets [11].

In this article, a correlation is established between the deficient wetting of grain boundaries and the presence of hydrogen introduced into the material during the hydrogen-decrepitation process. Two strategies are proposed to enhance the microstructure of microcrystalline Nd-Fe-B magnets prepared by the SPS. The first strategy involves thermally desorbing the hydrogen from the Nd-Fe-B powder before the SPS, with the aim of achieving a solidified-liquid network of the Nd-rich phase in the as-sintered state. The second strategy focuses on reducing the electrical currents in the sample, e.g., by wrapping the Nd-Fe-B material in tantalum foil, to prevent the decomposition of the $RE_2Fe_{14}B$ phase. The benefits of a reduced sintering temperature for improved high-temperature

Manuscript received 28 February 2024; revised 16 May 2024; accepted 18 June 2024. Date of publication 21 June 2024; date of current version 26 July 2024. Corresponding author: T. Tomše (e-mail: tomaz.tomse@ijs.si).

Color versions of one or more figures in this article are available at https://doi.org/10.1109/TMAG.2024.3417611.

Digital Object Identifier 10.1109/TMAG.2024.3417611

© 2024 The Authors. This work is licensed under a Creative Commons Attribution 4.0 License.
For more information, see https://creativecommons.org/licenses/by/4.0/

stability are demonstrated and the magnetic performance of the SPS samples sintered at ≈880 °C is compared with that of conventionally sintered magnets.

II. Experimental Procedure

Nd-Fe-B-type powder with the composition Fe-30.0Nd-3.0Co-1.0Dy-0.9B-0.6Pr-0.3O-0.2Ga-0.1Cu-0.1Al (wt.%) was provided by the company Magneti Ljubljana d.d. It was prepared via strip-casting, followed by hydrogen decrepitation and jet milling. The mean particle size of the powder was 6.8 μm.

To find the minimum temperature required to completely desorb the hydrogen from the Nd-Fe-B material, the powder was heated to 1000 °C with a 2 °C/min heating rate in a tube furnace (Carbolite) under a dynamic vacuum. Fig. 1 shows the pressure change during heating. The first peak at ≈170 °C corresponds to the desorption of hydrogen from the $RE_2Fe_{14}B$ matrix phase and partial desorption from the secondary Nd-rich phases, and the second peak at ≈580 °C to complete desorption from the Nd-rich phases [12]. Based on this result, the Nd-Fe-B powder was thermally degassed in a vacuum for 10 min at 600 °C before the SPS.

The SPS experiments were conducted in an SPS-632LxEx, Dr. SINTER (SPS Syntex Inc., Japan) furnace under a dynamic vacuum. For a typical run, 2 g of loose powder was placed into a cylindrical graphite die with an inner diameter of 10 mm and sealed under an argon atmosphere. A 200-μm-thick graphite foil was placed between the powder and the die/punches to provide good thermal and electrical contact and to prevent the liquid phase from damaging the graphite tools. In most cases, an additional 50-μm-thick tantalum foil was placed between the powder and the graphite foil. A schematic illustration of the Nd-Fe-B/Ta-foil/C-foil/die setup (cross-sectional view) is shown in Fig. 2(a). Before the SPS, the powder in the die was magnetically aligned along the longitudinal axis in a pulsed magnetic field of 6 T. A constant pressure of 50 MPa was applied uniaxially to the punches during the heating. A dc current with a 12:2 on-off pulse sequence (12 × 3.3 ms ≈ 0.04 s of current, followed by 2 × 3.3 ms ≈ 0.007 s of pause) was applied to heat the Nd-Fe-B material. The heating process was temperature-controlled using a K-type thermocouple inserted into the die. The heating rate was 50 °C/min. During heating, the vertical ram displacement corresponding to the Nd-Fe-B shrinkage and thermal expansion of the setup was monitored. Fig. 2(b) shows the die temperature (dashed curve) and the ram displacement (full curve) for a typical SPS run. The heating was terminated at approximately 880 °C when the ram displacement visibly started to level off. This is further seen in the derivative of the ram displacement curve in Fig. 2(c) showing a continuous drop in the shrinkage rate starting at ≈830 °C, indicating the final stage of densification. After the heating was terminated, the pressure applied to the sample was released. The procedure was optimized to prevent a partial loss of a liquid phase that was observed on the graphite punches with further temperature increase, resulting in additional small but steady ram displacement (not shown). The total heating time was 17 min. The heating cycle was followed by cooling.

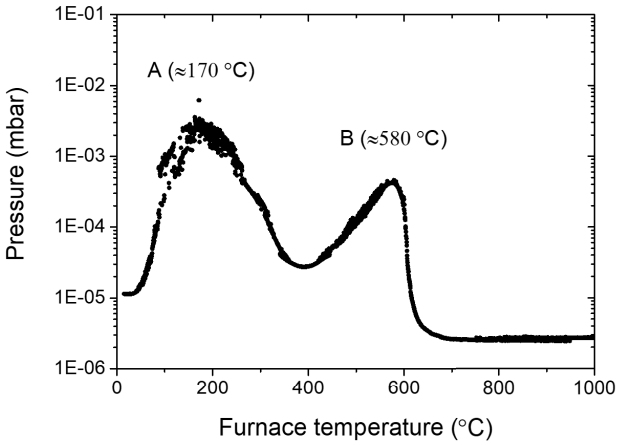

Fig. 1. Pressure change during heating of the Nd-Fe-B powder at 2 °C/min of heating rate in vacuum (A) desorption of hydrogen from $RE_2Fe_{14}B$ matrix phase and partial desorption from Nd-rich phase and (B) complete desorption from Nd-rich phase [12].

The effect of the SPS conditions on the microstructure formation and the intrinsic coercivity was studied for SPS samples prepared from loose powder. To compare the SPS approach with conventional sintering in terms of remanence and maximum energy product, one SPS sample and conventionally sintered samples were produced from powder compacts. The compacts were prepared from a thermally degassed powder by magnetically aligning it in a silicon mold with a pulsed field of 6 T, followed by isostatic pressing at 800 MPa.

Conventional sintering and post-sinter annealing (PSA) were performed in a tube furnace (Carbolite) under a 5×10^{-5} mbar vacuum. The sintering involved heating a powder compact at 3 °C/min from room temperature to 1070 °C. The dwell time was 120 min. For the PSA trials, the temperature varied between 420 °C and 920 °C and the heating time was 120 min.

The absolute densities of the samples were determined using Archimedes' principle with a density meter (Densitec) by immersing them in silicone oil. Microstructural analyses of the samples were conducted utilizing a field-emission-gun scanning electron microscope (FEG-SEM) JEOL JSM-7600F equipped with an energy-dispersive X-ray spectroscopy (EDS) detector (INCA system, Oxford Instruments, U.K.). Backscattered-electron (BSE) imaging in compositional contrast mode was employed to observe the major crystal phases. For the analysis, the samples were embedded in resin (EpoFix Kit Resin and hardener from Struers) and polished using isopropanol-based suspensions of 3- and 0.25-μm diamond paste. Polished surfaces of selected samples underwent chemical etching with an HCl-saturated Cyphos IL 101 ionic liquid to expose the grain boundaries. Surface etching selectively removed the secondary Nd-rich phases due to the highly negative reduction potential of the neodymium (−2.32 V) [13]. The apparent average grain size was determined from SEM images by measuring the diameters of 200 gr. This diameter represents the average projected grain diameter in the 2-D image. Assuming equiaxed grains, the actual grain size was estimated by multiplying the measured grain size by a

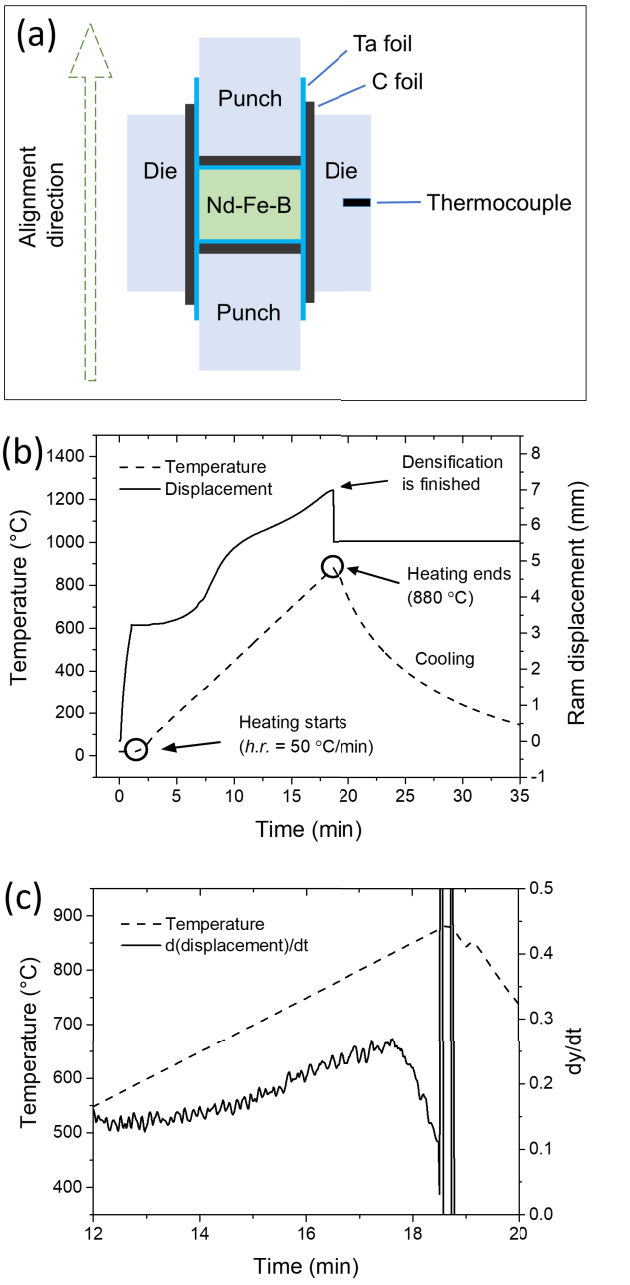

Fig. 2. (a) Cross-sectional (2-D) view of the Nd-Fe-B/Ta-foil/C-foil/die setup. (b) Example of an SPS process: measured temperature of the die (dashed curve) and vertical ram displacement corresponding to the Nd-Fe-B shrinkage and thermal expansion of the setup (full curve). (c) Derivative of the displacement curve in the final densification stage.

stereological correction factor of 1.5. Magnetic measurements at room temperature to 125 °C were conducted using a closed-loop hysteresisgraph (Permagraph, Magnet-Physik).

III. Results and Discussion

Table I lists selected bulk samples prepared under different conditions and the corresponding powder type (nondegassed; NDG, degassed: DG, and powder compact: PC), use of Ta foil, bulk density (ρ), and as-sintered magnetic properties: intrinsic coercivity (H_{ci}), remanence (B_r), and maximum energy product ($(BH)_{max}$). SPS sample A was prepared without Ta foil from nondegassed Nd-Fe-B powder. SPS sample B was prepared with Ta foil from nondegassed powder. SPS sample C was prepared with Ta foil from degassed powder. Note that its H_{ci} value serves as a representative figure, considering it is one among nine samples prepared under such conditions for further PSA study; the individual H_{ci} values of these samples ranged from 1010 to 1195 kA/m. SPS sample D was prepared with Ta foil from a powder compact. The conventionally sintered sample CS was prepared from a powder compact.

TABLE I
Specifics of Bulk Samples

Sample	Powder Type	Ta foil	ρ (g/cm^3)	H_{ci} (kA/m)	B_r (T)	$(BH)_{max}$ (kJ/m^3)
A	NDG	No	7.63	20	0.4	4
B	NDG	Yes	7.61	120	0.66	21
C	DG	Yes	7.62	1140	0.83	115
D	PC	Yes	7.60	950	1.05	203
CS	PC	/	7.58	770	1.23	291

Bulk samples prepared by SPS (A-D) and via conventional sintering (CS) with corresponding Nd-Fe-B powder type (non-degassed, NDG; degassed, DG; and powder compact, PC), use of Ta foil, bulk density (ρ), and as-sintered magnetic properties: intrinsic coercivity (H_{ci}), remanence (B_r), and maximum energy product ($(BH)_{max}$).

A. Microstructure

Fig. 3 shows BSE SEM images taken on polished cross sections of bulk SPS samples (samples A, B, and C) and a conventionally sintered sample CS. As shown in Fig. 3(a) and confirmed with EDS analyses at several locations, the microstructure of sample A consists of the matrix phase (gray contrast), Nd-rich phases with varying oxygen content (bright contrast), and α-Fe phase (dark contrast). α-Fe is a pro-peritectic soft-magnetic phase and is detrimental to the magnetic properties [14], [15]. According to the Nd-Fe-B phase diagram, the peritectic reaction takes place at ≈1180 °C, while the SPS was applied at ≈880 °C. Note that this is the temperature of the die and the actual sample's temperature is not known. The presence of α-Fe in the microstructure indicates local decomposition of the $Nd_2Fe_{14}B$ matrix phase during the SPS, resulting from Joule overheating at the particle-particle contacts, as reported in [10]. In contrast, the SPS samples B and C (Fig. 3(b) and (c), respectively), as well as the conventionally sintered sample CS [Fig. 3(d)] consists of the matrix phase and Nd-rich phases, but no α-Fe. Samples A and B were both prepared from the nondegassed powder and the important difference in the processing conditions between them was the use of Ta foil in the case of sample B. As demonstrated in [10], the decomposition of the $Nd_2Fe_{14}B$ matrix phase can be prevented by reducing the heating rate, which effectively reduces the electrical currents during the SPS. To explain the effect of Ta foil on the distribution of the electrical currents in the SPS setup, the electrical conductivity of the materials and the contact resistances are considered. First, the room-temperature electrical conductivity of tantalum is ≈8×10^6 S/m [16]. In comparison, the conductivity of the Nd-Fe-B is ≈7×10^5 S/m [17], i.e., an order of magnitude lower. Second, Ta foil placed between the sample and the graphite foil introduces additional electrical contact resistance into the system. Electrical contact resistances between the graphite die/punches and the sample affect the distribution

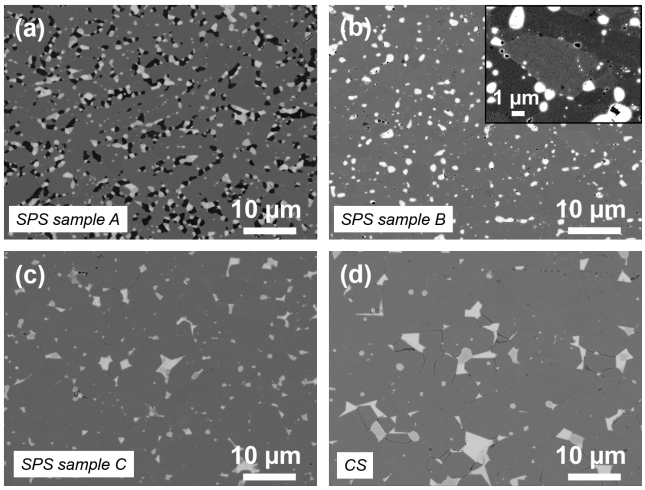

Fig. 3. BSE-SEM images taken from polished cross sections. (a) SPS sample A prepared from nondegassed powder without Ta foil. (b) SPS sample B prepared from nondegassed powder with Ta foil. (c) SPS sample C prepared from degassed powder with Ta foil. (d) Conventionally sintered sample CS.

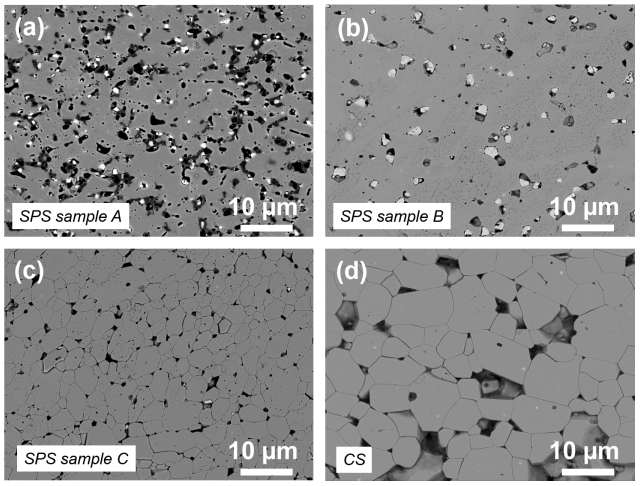

Fig. 4. BSE-SEM images of etched cross sections (a) SPS sample A, (b) SPS sample B, (c) SPS sample C, and (d) conventionally sintered sample CS.

of the current in an SPS setup [18]. In summary, Ta foil decreases the electrical currents in the sample either by ensuring preferential current flowthrough the graphite die/punches due to additional contact resistance, or by preferential current flowthrough the Ta foil. Further work is needed to understand its effect on the distribution of the temperature and current in the setup.

Concerning the effect of hydrogen on the microstructure formation, a notable difference between the microstructures shown in Fig. 3(b) and (c) is the shape of the bright Nd-rich grains in the triple junctions. In Fig. 3(b) (sample B prepared from nondegassed powder), the round shape of the grains indicates a large dihedral angle, which implies poor grain-boundary wetting [19]. As seen in the higher magnification image in the inset in Fig. 3(b), the Nd-rich phase is also observed along the grain boundaries as distinct sub-micrometer grains. In contrast, the Nd-rich grains in the triple junctions in Fig. 3(c) (sample C prepared from degassed powder) have small dihedral angles, indicating improved wetting. A similar microstructure is observed in Fig. 3(d) (conventionally sintered sample).

For the SPS samples prepared from nondegassed powder, i.e., samples A and B, whose etched microstructures (BSE-SEM images) are shown in Fig. 4(a) and (b), respectively, surface etching did not expose the grain boundaries, indicating a lack of Nd-rich grain boundary phase. In contrast, a solidified-liquid network and faceted grains are observed for SPS sample C and the conventionally sintered sample CS (Fig. 4(c) and (d), respectively), after etching. Such a microstructure is typical of solution-reprecipitation stage densification in liquid-phase sintering [19]. Importantly, the oxygen content in the four samples was similar at 0.32–0.33 wt.%. Therefore, the absence of a liquid phase in samples A and B cannot be attributed to oxidation during sintering.

In summary, SEM analyses of the bulk samples confirmed that the poor grain-boundary wetting is related to the presence of hydrogen in the Nd-Fe-B alloy. It is important to note that the hydrogen does not pose a problem for conventional sintering, even when Nd-hydrides are purposefully added to the base Nd-Fe-B powder, as it will desorb during the slow heating before the onset of liquid-phase sintering [20]. In contrast, the nonequilibrium conditions during rapid heating in the SPS kinetically inhibit hydrogen desorption.

B. Magnetic Performance

Second-quadrant demagnetization curves obtained at room temperature for samples A (gray), B (red), C (blue), D (green), and CS (black) are shown in Fig. 5. The corresponding magnetic properties are in Table I. Concerning the intrinsic coercivity, preventing the formation of α-Fe increased the H_{ci} value from 20 (sample A) to 120 kA/m (sample B); however, a more substantial improvement was achieved with the thermal desorption of the hydrogen before applying the SPS (1140 kA/m for sample C), which is attributed to the improved grain-boundary wetting, necessary to decouple the grains in terms of short-range exchange interactions across the grain boundaries [21]. On the one hand, the as-sintered H_{ci} value of sample C exceeds the intrinsic coercivity of sample CS (770 kA/m) by almost 50%. On the other hand, its modest B_r value at 0.83 T is only 67% of that measured for the conventionally sintered sample (1.23 T). Sample C was prepared from loose powder that was magnetically aligned before SPS. However, before the heating was initiated, the powder was first compressed under 50 MPa of pressure. As seen in Fig. 2(b), the corresponding initial ram displacement (full curve) was significant, amounting to 45% of the total ram displacement at the end of densification. Hence, the alignment of the particles was greatly affected, which explains the low remanence. However, for a powder compact consolidated with the SPS (sample D), the remanence was increased to 1.05 T, i.e., 85% of the B_r value of sample CS. The maximum energy products were 203 and 291 kJ/m^3 for samples D and CS, respectively. As reported in an earlier paper [11], analyses of the $Nd_2Fe_{14}B$ grain orientation via the electron backscatter diffraction (EBSD) confirmed that the uniaxially applied pressure during SPS weakens the texture in the SPS magnets compared to conventionally sintered ones.

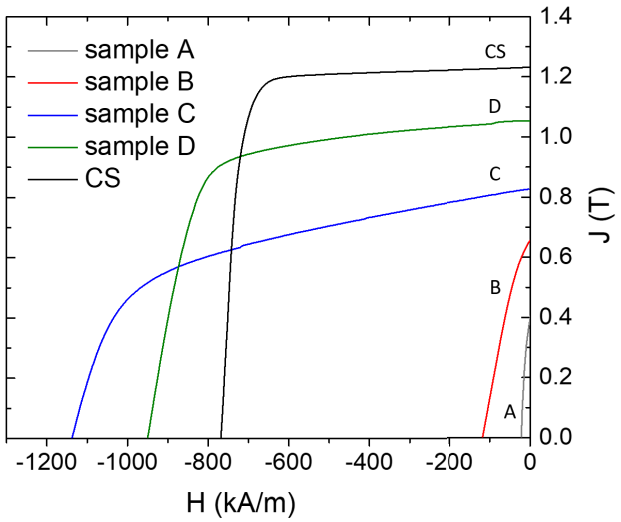

Fig. 5. Second-quadrant demagnetization curves of bulk samples (measured at room temperature).

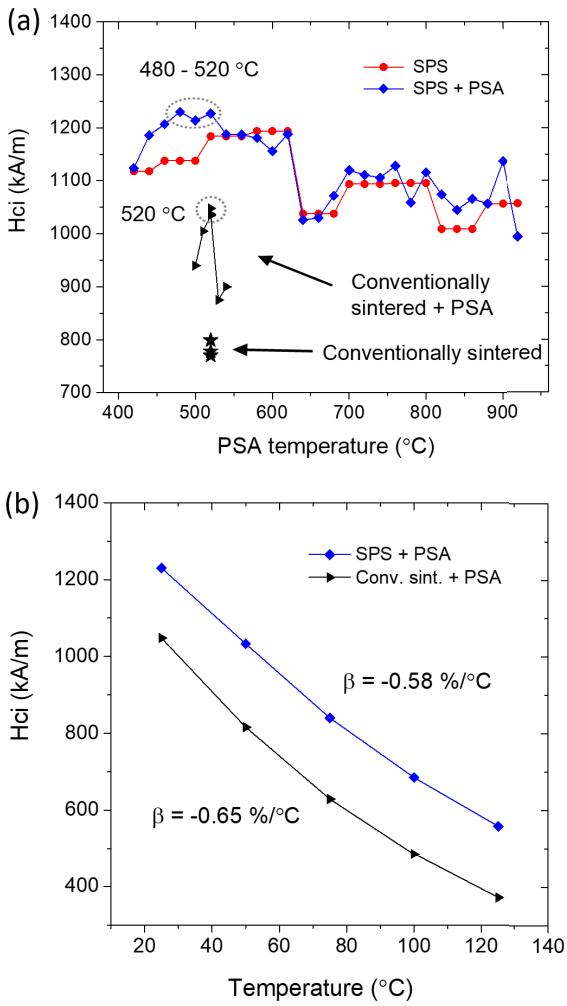

Fig. 6. (a) Dependence of SPS samples' intrinsic coercivity (squares) on the PSA temperature. The heating time was 120 min. Initial H_{ci} of SPS samples (circles), initial H_{ci} of conventionally sintered samples (stars), and H_{ci} of conventionally sintered samples post-sinter annealed at different temperatures (triangles) are added for comparison. (b) Temperature dependence of intrinsic coercivity of an optimally post-sinter annealed SPS sample (squares) and a conventionally sintered sample (triangles).

The as-sintered H_{ci} values give only limited information on the material's potential for high performance. Irregularities at the interfaces between the thin grain-boundary film and the matrix grains due to the swift solidification of the liquid phase following the sintering process can impede the formation of coercivity [22], [23]. PSA is necessary to maximize the coercivity by eliminating structural distortions and redistributing the grain-boundary phase. The effect of the annealing temperature on the coercivity was investigated. The initial as-sintered coercivities of the SPS samples prepared from degassed Nd-Fe-B powder (red circles, 1010–1195 kA/m), as-sintered coercivities of conventionally sintered samples (black stars, 770–800 kA/m), and the PSA H_{ci} values of the SPS (blue squares) and conventionally sintered samples (black triangles) are compared in Fig. 6(a). Over the range of 420 °C–920 °C, the largest coercivity increase after PSA (4%–8%) and the highest final H_{ci} values (1215–1230 kA/m) were observed between 480 °C and 520 °C for SPS samples. Such PSA temperatures are typical for sintered Nd-Fe-B magnets [24]. On the other hand, for conventionally sintered samples, the PSA H_{ci} values peaked at 520 °C and reached 1035–1050 kA/m for three different samples, signifying a 31%–34% increase in their as-sintered coercivities.

In summary, for the optimally post-sinter annealed SPS samples with favorable phase composition and distribution of the grain-boundary phase in the as-sintered state, the H_{ci} values exceeded that of conventionally sintered and post-sinter annealed magnets by more than 15%. On the one hand, this is attributed to the difference in the grain size. A comparison of the etched microstructures of the SPS and conventionally sintered samples (Fig. 4(c) and (d), respectively) revealed that the grains were smaller in the former. The average grain size was estimated at 9.3 and 14.0 μm for samples C and CS, respectively. This ≈33% reduction in grain size of fully dense, sintered Nd-Fe-B magnets is ascribed to the low SPS sintering temperature (≈880 °C). On the other hand, because the coercivity of the samples prepared here is much weaker than the anisotropy field of the $Nd_2Fe_{14}B$ intermetallic system, magnetization reversal in each grain through nucleation of reverse domains follows the $1/\cos\theta$ law [25]. Therefore, the higher H_{ci} values of the SPS samples are partially attributed to their lower texture. Correspondingly, the lower H_{ci} value of sample D compared to sample C (950 and 1140 kA/m, respectively, Table I) is attributed to an improved degree of alignment in accordance with ≈25% higher B_r value.

Reduction in grain size observed for SPS sample C favorably affected the temperature coefficient of coercivity (β) calculated as $\Delta H_{ci}/(H_{ci}(25\ °C)\Delta T) \times 100$ for the 25 °C–125 °C range. As seen in Fig. 6(b), the coercivity drops when the temperature is increased. This trend, to an extent, reflects the temperature dependence of the anisotropy field of the $RE_2Fe_{14}B$ hard-magnetic phase [26]. The calculated β values are −0.58%/°C and −0.65%/°C for the SPS and conventionally sintered magnet.

The maximum coercivity of the SPS samples reported here (1230 kA/m) is higher than the values reported in [7] and [9] (1165 and 1218 kA/m, respectively) and lower than

in [8] and [11] (1651 and 1385 kA/m, respectively). However, coercivity depends heavily on the magnets' chemical composition. The rare-earth content in [7], [8], and [9] was ≈35 wt.%, much higher than the 31.6 wt.% in this study. Moreover, the Dy content was 2.0 and 3.4 wt.% in [8] and [11], respectively, and 1 wt.% here. Higher rare-earth and dysprosium contents are both beneficial for the development of coercivity. A major coercivity-limiting factor for the SPS and conventionally sintered magnets is the initial mean powder particle size (≈6.8 μm), which should be reduced to around 3 μm to maximize the magnetic properties [27].

IV. Conclusion

In this study, a microcrystalline, anisotropic, Nd-Fe-B powder prepared by standard procedures was consolidated to full density with the SPS at lower temperatures and with greatly reduced heating times compared to conventional sintering. Hence, the grain growth was inhibited and the high-temperature performance was improved. Although the samples had a simple disk-shaped geometry, an important advantage of the SPS compared to conventional sintering is its potential for the net-shape manufacture of products with more intricate shapes [28]. The prospect of solving the design constraints of sintered magnets could pave the way for advances in the design and efficiency of electrical motor systems [29], [30]. A major challenge related to the SPS that needs to be addressed is the deterioration of the crystallographic texture, which adversely affects the remanence and the energy product. However, reducing the pressure applied to the sample during the SPS can minimize its negative effect on the grain alignment [7], which should be considered for the future development of SPS-based sintering strategies for Nd-Fe-B powders.

Acknowledgment

The authors would like to thank Dr. Paul McGuiness for proofreading. This work was supported in part by the Slovenian Research Agency under Grant P2-0084 and Grant Z2-2645, in part by the European Institute of Innovation and Technology (EIT) RAW Materials RECO2MAG under Grant 21043, and in part by European Union's Horizon Europe Research and Innovation program REESILIENCE under Grant 101058598.

References

[1] M. Sagawa, S. Fujimura, N. Togawa, H. Yamamoto, and Y. Matsuura, "New material for permanent magnets on a base of Nd and Fe (invited)," *J. Appl. Phys.*, vol. 55, no. 6, pp. 2083–2087, Mar. 1984.

[2] O. Gutfleisch, M. A. Willard, E. Brück, C. H. Chen, S. G. Sankar, and J. P. Liu, "Magnetic materials and devices for the 21st century: Stronger, lighter, and more energy efficient," *Adv. Mater.*, vol. 23, no. 7, pp. 821–842, Feb. 2011.

[3] K. Uestuener, M. Katter, and W. Rodewald, "Dependence of the mean grain size and coercivity of sintered Nd–Fe–B magnets on the initial powder particle size," *IEEE Trans. Magn.*, vol. 42, no. 10, pp. 2897–2899, Oct. 2006.

[4] J. Fidler and T. Schrefl, "Overview of Nd–Fe–B magnets and coercivity," *J. Appl. Phys.*, vol. 79, no. 8, pp. 5029–5034, 1996.

[5] H. Sepehri-Amin, Y. Une, T. Ohkubo, K. Hono, and M. Sagawa, "Microstructure of fine-grained Nd–Fe–B sintered magnets with high coercivity," *Scripta Mater.*, vol. 65, no. 5, pp. 396–399, Sep. 2011.

[6] O. Guillon et al., "Field-assisted sintering technology/spark plasma sintering: Mechanisms, materials, and technology developments," *Adv. Eng. Mater.*, vol. 16, no. 7, pp. 830–849, Jul. 2014.

[7] M. Yue, J. Zhang, Y. Xiao, G. Wang, and T. Li, "New kind of NdFeB magnet prepared by spark plasma sintering," *IEEE Trans. Magn.*, vol. 39, no. 6, pp. 3551–3553, Nov. 2003.

[8] M. Yue, A. Cao, G. Wang, W. Liu, and J. Zhang, "Mechanical properties of spark plasma sintering Nd–Fe–B permanent magnets," *Phys. Status Solidi A*, vol. 204, no. 12, pp. 4149–4152, Dec. 2007.

[9] W. Mo, L. Zhang, A. Shan, L. Cao, J. Wu, and M. Komuro, "Microstructure and magnetic properties of NdFeB magnet prepared by spark plasma sintering," *Intermetallics*, vol. 15, no. 11, pp. 1483–1488, Nov. 2007.

[10] T. Tomše et al., "Unravelling the intricacies of micro-nonuniform heating in field-assisted sintering of multiphase metallic microstructures," *J. Mater. Process. Technol.*, vol. 328, Jul. 2024, Art. no. 118405.

[11] T. Tomše et al., "A spark-plasma-sintering approach to the manufacture of anisotropic Nd-Fe-B permanent magnets," *J. Magn. Magn. Mater.*, vol. 502, May 2020, Art. no. 166504.

[12] A. J. Williams, P. J. McGuiness, and I. R. Harris, "Mass spectrometer hydrogen desorption studies on some hydrided NdFeB-type alloys," *J. Less Common Met.*, vol. 171, no. 1, pp. 149–155, Aug. 1991.

[13] L. Schultz, A. M. El-Aziz, G. Barkleit, and K. Mummert, "Corrosion behaviour of Nd–Fe–B permanent magnetic alloys," *Mater. Sci. Eng. A*, vol. 267, no. 2, pp. 307–313, Jul. 1999.

[14] Y. Matsuura, S. Hirosawa, H. Yamamoto, S. Fujimura, M. Sagawa, and K. Osamura, "Phase diagram of the Nd-Fe-B ternary system," *Jpn. J. Appl. Phys.*, vol. 24, no. 8A, Aug. 1985.

[15] J. Herbst, "R2Fe14B materials: Intrinsic properties and technological aspects," *Rev. Mod. Phys.*, vol. 63, no. 4, p. 819, 1991.

[16] M. Cox, "Thermal and electrical conductivities of tungsten and tantalum," *Phys. Rev.*, vol. 64, nos. 7–8, pp. 241–247, Oct. 1943.

[17] Accessed: Feb. 1, 2024. [Online]. Available: https://e-magnetsuk.com/introduction-to-neodymium-magnets/characteristics-of-ndfeb-magnets/

[18] K. Vanmeensel, A. Laptev, J. Hennicke, J. Vleugels, and O. Vanderbiest, "Modelling of the temperature distribution during field assisted sintering," *Acta Mater.*, vol. 53, no. 16, pp. 4379–4388, Sep. 2005.

[19] R. M. German, P. Suri, and S. J. Park, "Liquid phase sintering," *J. Mater. Sci.*, vol. 44, pp. 1–39, Jan. 2009.

[20] T. Ma et al., "Grain boundary restructuring of multi-main-phase Nd-Ce-Fe-B sintered magnets with nd hydrides," *Acta Mater.*, vol. 142, pp. 18–28, Jan. 2018.

[21] K. Hono and H. Sepehri-Amin, "Strategy for high-coercivity Nd–Fe–B magnets," *Scripta Mater.*, vol. 67, no. 6, pp. 530–535, Sep. 2012.

[22] P. J. McGuiness, A. J. Williams, I. R. Harris, E. Rozendaal, and J. Ormerod, "Sintering behaviour of NdFeB magnets," *IEEE Trans. Magn.*, vol. 25, no. 5, pp. 3773–3775, Sep. 1989.

[23] F. Vial, F. Joly, E. Nevalainen, M. Sagawa, K. Hiraga, and K. T. Park, "Improvement of coercivity of sintered NdFeB permanent magnets by heat treatment," *J. Magn. Magn. Mater.*, vols. 242–245, pp. 1329–1334, Apr. 2002.

[24] V. P. Menushenkov and A. G. Savchenko, "Effects of post-sintering annealing on magnetic properties of Nd–Fe–B sintered magnets," *J. Magn. Magn. Mater.*, vols. 258–259, pp. 558–560, Mar. 2003.

[25] D. Givord, P. Tenaud, and T. Viadieu, "Angular dependence of coercivity in sintered magnets," *J. Magn. Magn. Mater.*, vol. 72, no. 3, pp. 247–252, Apr. 1988.

[26] M. Sagawa et al., "Dependence of coercivity on the anisotropy field in the $Nd_2Fe_{14}B$-type sintered magnets," *J. Appl. Phys.*, vol. 61, no. 8, pp. 3559–3561, Apr. 1987.

[27] W. F. Li, T. Ohkubo, K. Hono, and M. Sagawa, "The origin of coercivity decrease in fine grained Nd–Fe–B sintered magnets," *J. Magn. Magn. Mater.*, vol. 321, no. 8, pp. 1100–1105, Apr. 2009.

[28] C. Manière, E. Nigito, L. Durand, A. Weibel, Y. Beynet, and C. Estournès, "Spark plasma sintering and complex shapes: The deformed interfaces approach," *Powder Technol.*, vol. 320, pp. 340–345, Oct. 2017.

[29] K.-C. Kim, S.-B. Lim, D.-H. Koo, and J. Lee, "The shape design of permanent magnet for permanent magnet synchronous motor considering partial demagnetization," *IEEE Trans. Magn.*, vol. 42, no. 10, pp. 3485–3487, Oct. 2006.

[30] B. Podmiljšak et al., "The future of permanent-magnet-based electric motors: How will rare earths affect electrification?" *Materials*, vol. 17, no. 4, p. 848, Feb. 2024.